Tellus (2000), 52A, 347–364
Printed in UK. All rights reserved

TELLUS
ISSN 0280–6495

Synoptic climatology of Northern Hemisphere available potential energy collapses

By WERNER WINTELS* and JOHN R. GYAKUM, *Department of Atmospheric and Oceanic Sciences, McGill University, Montreal, Canada*

(Manuscript received 25 May 1999; in final form 21 December 1999)

ABSTRACT

Three recurring regional patterns of extratropical baroclinic development associated with synoptic-scale collapses of Northern Hemisphere available potential energy (APE) are identified using a 1979–95 time series derived from the National Centers for Environmental Prediction (NCEP) reanalysis. A time series of the intraseasonal signal (from 1.6 to 180 days) of APE is used to discern an average cycle of approximately 3 days in the APE generation rate $\mathrm{d}A/\mathrm{d}t$ (referred to as APE depletion rate if negative). An APE depletion event is defined as a fall and subsequent rise in the time series of $\mathrm{d}A/\mathrm{d}t$ associated with this cycle. We define synoptic-scale APE collapses as APE depletion events with maximum depletion rates ($\mathrm{d}A/\mathrm{d}t_{\mathrm{min}}$) and maximum APE falls (ΔA_{min}) of less than -0.145×10^6 J m^{-2} day^{-1} and -0.280×10^6 J m^{-2}, respectively. All are cold season (15 October–15 April) events. APE collapses were classified based on the evolution of regional synoptic patterns during the 2 days centered at the time of $\mathrm{d}A/\mathrm{d}t_{\mathrm{min}}$. All are accompanied by deep tropospheric warming. The west Pacific warm surge (Type A) is driven by cyclogenesis over Japan and anticyclogenesis over the west-central North Pacific. The Bering warm surge (Type B) is associated with an intense southerly flow across the Bering Strait brought on by cyclogenesis near the Kamchatka Peninsula and an intense anticyclone over Alaska. The Atlantic Canada warm surge (Type C) is characterized by an onshore flow of warm air ahead of a continental storm track over eastern North America.

1. Introduction

Available potential energy (APE) represents a fundamental quantity that can be used to gauge the effect of transient baroclinic eddies upon the planetary circulation. Margules (1903) first described APE as the portion of the atmosphere's potential and internal energy that can be converted to kinetic energy (KE). Lorenz (1955) derived an approximate expression in pressure coordinates:

$$A = \frac{1}{2}\int_0^{p_{\mathrm{sfc}}} \bar{T}(\Gamma_{\mathrm{d}} - \bar{\Gamma})^{-1}\,\frac{\overline{(T-\bar{T})^2}}{\bar{T}^2}\,\mathrm{d}p, \qquad (1)$$

where A is APE, T is the temperature, $\Gamma = -\partial T/\partial z$ the lapse rate, and Γ_{d} the dry adiabatic lapse rate; the over-bar denotes hemispheric averages, p indicates pressure and p_{sfc} indicates surface pressure. Although Lorenz's APE has physical meaning only within the context of an isolated 3-dimensional system, localized thermodynamic processes directly affect APE. Energy and thermodynamic budgets may be calculated for domains associated with individual cyclones and anticyclones (Lin and Smith, 1982) to assess their impact on the broader atmospheric system. The baroclinic conversion of APE, for example, is associated with localized overturning motion involving sinking cold air and rising warm air (Smith, 1969):

$$\left.\frac{\mathrm{d}A}{\mathrm{d}t}\right|_{\mathrm{adia}} = \int_{p_1}^{p_2}\int_{\sigma} \omega\alpha\,\mathrm{d}\sigma\,\mathrm{d}p, \qquad (2)$$

* Corresponding author.
e-mail: wintels@zephyr.meteo.mcgill.ca

σ represents the localized area of integration, ω is the vertical motion in pressure coordinates, α the specific volume, and p_1 and p_2 the upper and lower bounds of the column, respectively. This is equal to the generation of KE when globally integrated. Synoptic-scale eddies are responsible for the bulk of baroclinic energy conversions in the wintertime atmosphere (Peixoto and Oort, 1992). Sheng and Derome (1991) have shown that these energy conversions not only drive the mean flow, but also provide energy for low-frequency transients.

Synoptic-scale baroclinic conversions are difficult to resolve in general circulation models (GCMs). Siegmund (1995) has shown that GCMs tend to overestimate the localized diabatic generation of transient APE and, as a consequence, the baroclinic conversions associated with these disturbances. The effects of diabatic heating can be assessed in pressure coordinates (Smith, 1969):

$$\left.\frac{\mathrm{d}A}{\mathrm{d}t}\right|_{\mathrm{dia}} = \frac{c_\mathrm{p}}{g} \int_{p_1}^{p_2} \int_{\sigma} \frac{(p - p_\mathrm{r})^\kappa}{p^\kappa} Q \,\mathrm{d}\sigma \,\mathrm{d}p, \tag{3}$$

where p is the pressure, p_r the reference pressure, Q the rate of diabatic heating, c_p the specific heat at constant pressure, g the gravitation constant, and κ is $R_\mathrm{d}/c_\mathrm{p}$ (R_d the dry gas constant). The reference pressure is the mean globally integrated pressure on the isentropic surface passing through the point in question. The entire expression $(p - p_\mathrm{r})^\kappa/p^\kappa$ is called the efficiency factor (Dutton and Johnson, 1967), since it determines the sensitivity of global APE to local sensible heating. Near the poles, most isentropic surfaces tend to reside at higher elevations than their global mean; the efficiency factor is negative, and radiative cooling leads to APE increases. Conversely, the efficiency factor is positive in tropical air masses, so that latent heating increases the planetary APE. APE generation therefore depends on the location of diabatic heating with respect to existing thermal anomalies.

This study is motivated by the observation that the March 1993 Superstorm over eastern North America was accompanied by a noteworthy decrease in Northern Hemisphere (NH) APE (Bosart et al., 1996). A significant upstream anticyclone and continental cold surge into the Gulf of Mexico accompanied this development (Schultz et al., 1997). Orlanski and Sheldon (1995) described a robust localized baroclinic conversion associated with the growth of a KE center above the storm. Huo et al. (1995) show that latent heating contributes significantly to the storm's development, accounting for a large portion of the observed central pressure falls. It appears that latent heating plays an important rôle in the diagnosed energetics and observed collapse of APE.

The above results have potential implications for mid- to long-range forecasting. Cataclysmic falls in hemispheric APE imply that the atmosphere either releases kinetic energy or diabatically alters its thermal structure in bursts of synoptic-scale activity. If APE collapses are a sign of intense regional baroclinic development, then the synoptic structure, predictability, and the dynamical and physical processes associated with these events would be of considerable practical and theoretical importance. Such events should play a key rôle in climate, being associated with large-scale transient transports of heat across midlatitudes and strong fluxes of thermal energy into the atmospheric system. The inability to resolve these systems could lead to important errors in both forecasting and general circulation models. Sufficient data and accurate representation of the physics and dynamics would be particularly crucial in these regions.

The objectives of this study are: (a) to produce a time series of Northern Hemisphere APE and a statistically meaningful climatology of its intraseasonal variability; (b) to identify evidence of synoptic-scale variability in the APE time series; (c) to isolate regional patterns of transient baroclinic development associated with synoptic-scale APE collapses. In Section 2, we describe the data and methodology used to generate and analyze the 17-year time series of Northern Hemisphere APE used in this study. Section 3 contains a time-series analysis of the intraseasonal variance and a quantitative definition of synoptic-scale APE collapses. In Section 4, we examine the thermal and geopotential structure of the top 40 APE collapses. Results are summarized in Section 5.

2. Data and procedure

The National Centers for Environmental Prediction (NCEP) reanalysis (Kalnay et al., 1996) offers 6-hourly analyses of geopotential height, temperature, and winds at 17 pressure levels between 1000 and 10 hPa on a global 2.5 × 2.5 latitude–longitude grid. The data were obtained from the Climate Diagnostics Center (CDC). For composite and climatological studies, the NCEP reanalysis provides a consistent analysis procedure for the available years, a great advantage over the previous NCEP (formerly National Meteorological Center) operational analysis (Trenberth and Olson, 1988).

Eq. (1) was evaluated using the NCEP temperature data. This approximate expression has proven to be sufficient for the purpose of assessing planetary-scale integrals of APE, even though it tends to overestimate APE values in the lowest layer (Siegmund, 1994). Temperature anomalies were calculated on pressure levels. Lapse rates on pressure levels were determined using a weighted average of $\partial T/\partial p$ for adjacent atmospheric layers and converted to height coordinates:

$$\frac{\partial T}{\partial z} = -\frac{g}{R_d}\frac{\partial \ln T}{\partial \ln p}. \qquad (4)$$

On the 1000 hPa level, the 1000–925 hPa lapse rate was used. The APE for different hemispheric layers was then calculated, recorded, and integrated. For layers intercepted by the earth's surface, the integral weighting dp is the difference between the surface pressure (i.e., the pressure on the lowest model level of the NCEP reanalysis grid) and the lowest mandatory pressure level. Subterranean layers were not included in the integration.

The Fourier power spectrum (P) of the complete 1979–95 time series was calculated using:

$$P_k = \omega_k(a_k^2 + b_k^2), \qquad (5)$$

where $\omega_k = 2\pi k/L$ is the angular frequency of the kth Fourier mode, L is the duration of the time series, and a_k, b_k are the sine and cosine coefficients (Tolstov, 1962). The normalized power associated with a time scale defined by wavenumbers k_1 and k_2 is:

$$\langle P_{k_1,k_2}\rangle = \frac{\sum_{k=k_1}^{k_2} P_k}{\sum_{k=1}^{N/2} P_k}, \qquad (6)$$

where N is the number of points in the time series.

A 3-point smoother and band-pass Fourier filter were applied, removing the variance associated with diurnal, semi-annual, and annual diabatic forcing, retaining the intraseasonal signal between 1.6 to 180 days. Inspection of the resulting time series shows that this removes most of the effects of diabatic forcing (including aliasing). All subsequent analysis was performed upon this filtered data set between 1 February 1979 and 30 November 1995.

Composite height and thickness fields are calculated using the NCEP reanalysis data on 1000, 500, and 200 hPa pressure levels. Anomaly fields are based on a 1979–95 monthly climatology, linearly interpolated to the date in question. Statistical significance at 95% and 99% confidence levels for composite anomalies are calculated using the Student t-test (Freund, 1971).

3. Time series analysis

3.1. Intraseasonal variability of Northern Hemisphere APE

We search for evidence of a characteristic time scale of Northern Hemisphere APE variability. The normalized power spectrum in Fig. 1 shows that most variability occurs at annual and diurnal time scales. Spectral peaks appear at daily, semi-annual, and annual time scales. Each is linked to familiar effects of solar forcing. The daily signal is associated with the rotation of the Earth and the uneven longitudinal distribution of Northern Hemisphere landmasses. The annual and semi-annual signals are associated with strong seasonal and zonal differences in insolation. Only 3% of the normalized variability (eq. (6)) can be explained by intraseasonal (1.6–180 day) fluctuations. Most of this variability is observed at a monthly time scale between 10 and 50 days, peaking at 30 days.

Fig. 2 shows the raw time series of the APE data set. The mean and intraseasonal rms variance are calculated for 6-month warm and cold seasons:

$$\bar{A} = \sum_{i=1}^{N}\frac{A_i}{N}, \qquad A_{\rm rms} = \sqrt{\sum_{i=1}^{N}\frac{(A_i-\bar{A})^2}{N}}, \qquad (7)$$

where N is the number of values within a 6-month period. The dominance of the annual signal is apparent. Also visible is the wintertime intraseasonal variance and its dominant low-frequency time scale. The cold season (15 October–15 April)

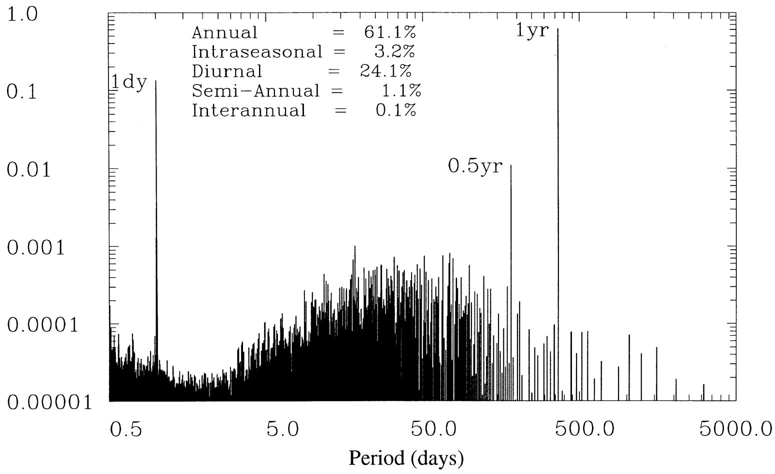

Fig. 1. Normalized power spectrum of Northern Hemisphere available potential energy (APE) 1979–95. Plotted on log–log scale. Percentage variance given for annual ($T=365$ days), intraseasonal ($T=1$–180 days), semi-annual ($T=182.5$ days), diurnal ($T=1$ day), and interannual ($T>365$ days) time scales.

mean (5.16×10^6 J m^{-2}) and intraseasonal variance (0.20×10^6 J m^{-2}) are double those of the warm season (15 April–15 October) values (2.72 and 0.11×10^6 J m^{-2}, respectively). The cold season rms variances show considerable interannual variability, with values ranging between 0.16 and 0.25. There is little to suggest the direct influence of synoptic-scale baroclinic waves, which are generally accepted to act on a time scale of 1 to 6 days.

3.2. *APE depletion events and synoptic-scale APE collapses*

Inspection of the time derivative of Northern Hemisphere APE reveals evidence of synoptic-scale variability. Fig. 3 shows 4-month traces of Northern Hemisphere APE and its time derivative dA/dt for the winters of 1988–89 and 1992–93. The value dA/dt is calculated using 24-h centered-difference APE tendencies:

$$\frac{dA}{dt}(t)=\frac{A(t+12\text{ h})-A(t-12\text{ h})}{1\text{ day}}, \qquad (8)$$

and will be referred to as the *APE generation (depletion) rate* when positive (negative). A clear cycle of falls and rises appears in the time series and is used to define *APE depletion events*. Each event is characterized by a minimum in the APE generation rate (dA/dt_{min}); minima are marked by upward-pointing arrows for 3 events identified as cases A, B, and C in Fig. 3. Adjacent local maxima, identified by downward pointing arrows, indicate the onset and termination times of these events. For the period between 1 February 1979 and 30 November 1995, 2200 APE depletion events were identified. Statistical analysis showed that the mean duration of an event is 2.80 days, with only a small number lasting longer than 5 days. This is consistent with time scales of commonly observed synoptic-scale eddies and baroclinic instability.

Cases A, B, and C represent 3 exceptional APE depletion events belonging to one of 3 patterns of regional baroclinic development. These are referred to as synoptic-scale APE collapses since they show exceptionally large values of dA/dt_{min} and are associated with large APE falls. Cases A and B, for example, coincide with a remarkable 14-day APE collapse of approximately 1.4×10^6 J m^{-2} between 22 January and 5 February 1989. This long-term collapse is the largest fall observed at any time-scale in our data set. Case C appears as an isolated event.

We formally define synoptic-scale APE collapses as APE depletion events that exceed negative threshold values of (a) -0.145×10^6 J m^{-2} day^{-1} for the maximum APE depletion rate (dA/dt_{min}); and (b) -0.280×10^6 J m^{-2} for APE fall (ΔA_{min}); ΔA_{min} represents the greatest negative change in

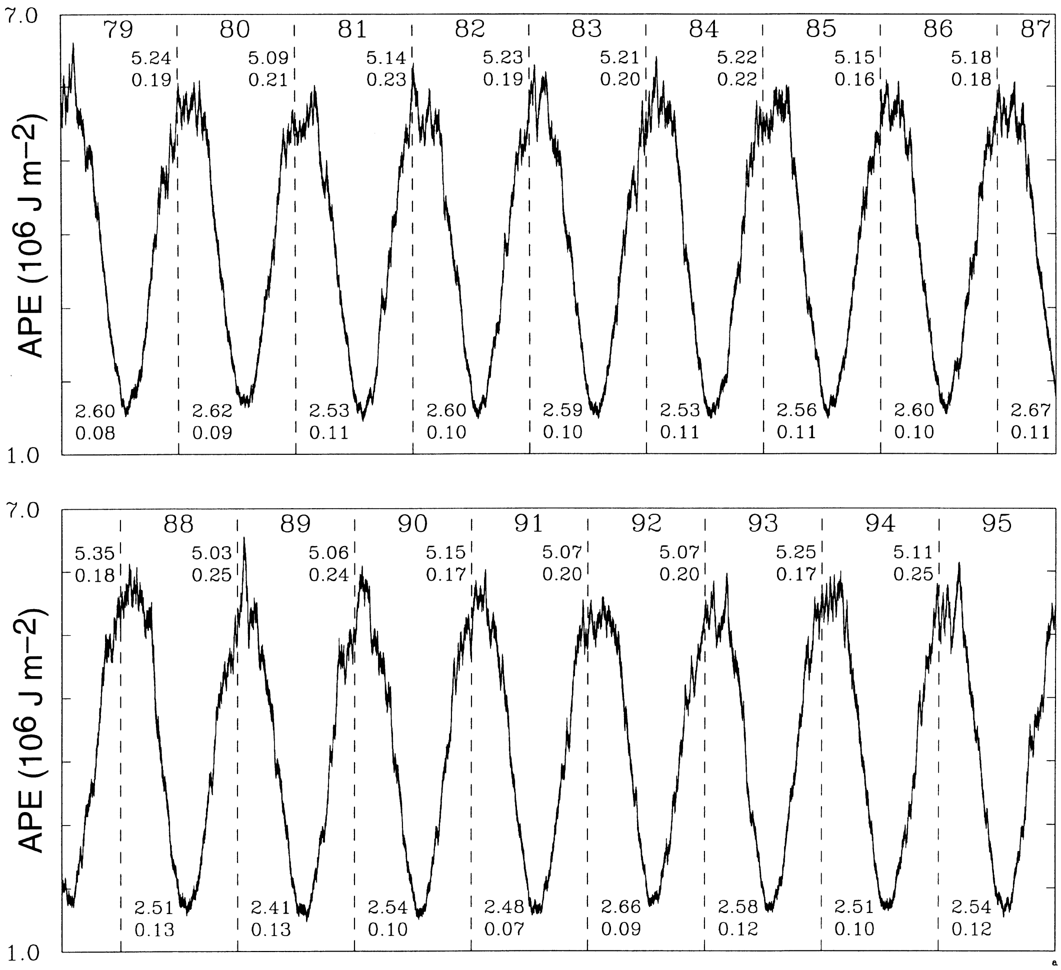

Fig. 2. Time series of Northern Hemisphere APE (10^6 J m^{-2}). Years shown at top of chart. Seasonal mean and intraseasonal rms variance for cold (15 October–15 April) and warm (15 April–15 October) seasons to left of respective seasonal extreme.

APE during a given depletion event:

$$\Delta A_{\min} = A(t_2) - A(t_1), \tag{9}$$

where t_1 and t_2 are times chosen so that ΔA is a minimum. These values are considerably larger than the mean values for all 2200 APE depletion events (0.03 J m^{-2} day^{-1} and 0.04 J m^{-2} for $dA/dt_{\min}$ and $\Delta A_{\min}$, respectively). The thresholds are chosen to generate a data set of 40 cases, sufficiently large to allow for stratification into statistically significant subsets. Each case falls within the top 60 events (ca. the 2.5 percentile) according to either parameter.

Whereas choosing events with large dA/dt is meant to isolate the signatures of the most significant transient synoptic waves, choosing events with large ΔA assures that periods of strong APE depletion are sustained long enough to effect large-scale changes in the atmospheric thermal structure and the hemispheric circulation. Fig. 3 illustrates this rationale. The 3 identified APE collapses show a large decrease in APE over the course of a few

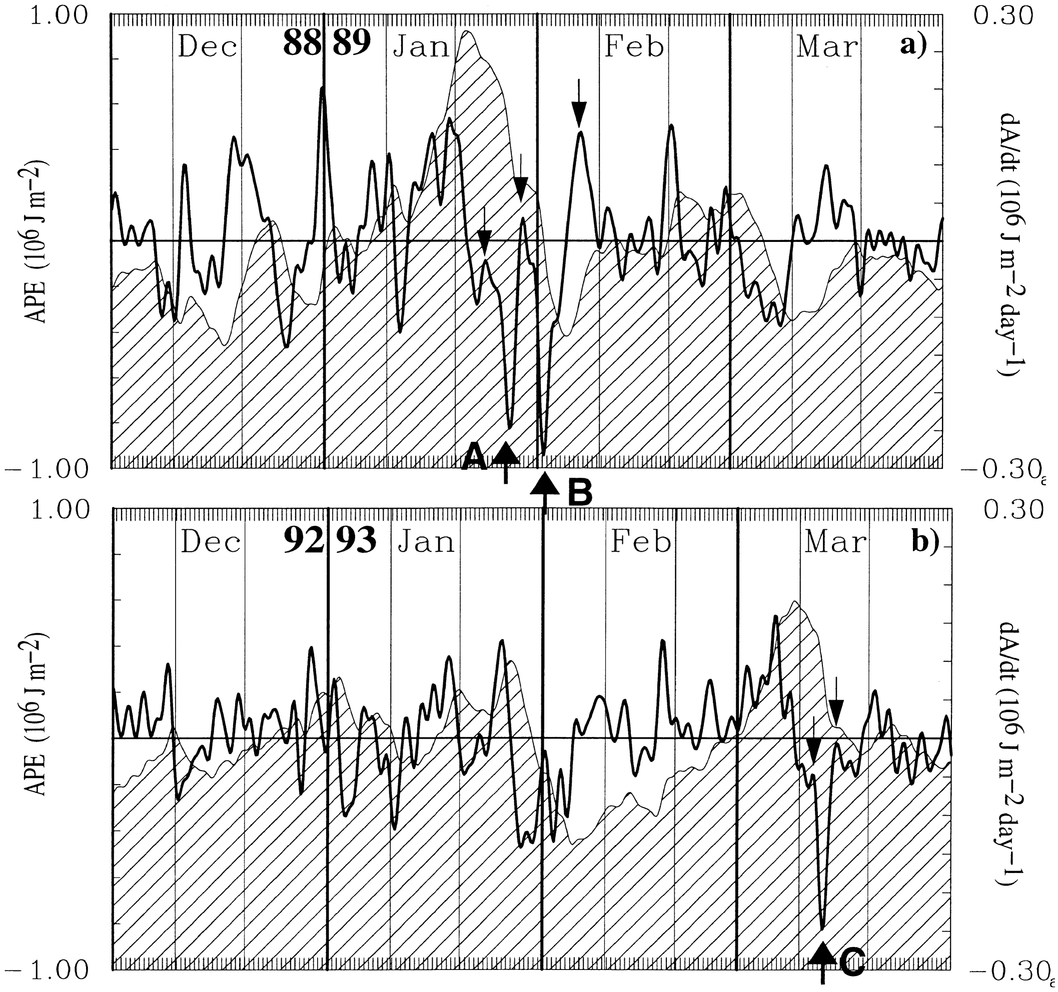

Fig. 3. Time series of detrended Northern Hemisphere APE (shaded) and APE generation rate dA/dt (bold) for winters (a) 1988–89 and (b) 1992–93. APE depletion event defined as cycle comprising fall and rise of dA/dt. Arrows indicate local maxima in APE depletion rate (dA/dt_{min}).

days and are each dominated by individual events showing large depletion rates. The appreciable collapse initiated at the end of January 1993 is not included because dA/dt_{min} during the APE collapse never exceeds the threshold value; no single synoptic-scale event dominates.

Table 1 lists the dates, dA/dt_{min}, and ΔA_{min} for the 40 identified APE collapses. Fig. 4 presents this data in graphical form. All 40 cases are cold-season events with a preference for the winter months (Fig. 4a). No clear trend can be discerned in the interannual data (Fig. 4b). APE collapses last between 3 and 8 days (Fig. 4c), persisting on average 2 days longer than the typical 3-day cold-season event; this suggests that the life cycle of synoptic-scale waves associated with these events may be longer than the 2 to 3 day modes typically assigned to baroclinic instability.

For the purposes of compositing, the times of dA/dt_{min} shown in Table 1 are chosen as $T = 0$. The time series of the composite collapse is shown in Fig. 5. Error bars represent the standard

Table 1. *Statistics for 40 APE collapses*

ID	$T=0$	ΔT	$\mathrm{d}A/\mathrm{d}t_{\min}$	$\Delta\mathrm{APE}_{\min}$	Category	ID	$T=0$	ΔT	$\mathrm{d}A/\mathrm{d}t_{\min}$	$\Delta\mathrm{APE}_{\min}$	Category
1	89 02 01 18	7.00	−0.283	−0·637	B[1]	21	87 11 17 12	5.75	−0.172	−0.343	A C
2	89 01 27 18	5.50	−0.248	−0.572	A[1] C	22	83 04 14 18	3.75	−0.172	−0.308	A
3	93 03 13 06	3.50	−0.248	−0.428	C[1]	23	84 02 06 06	2.75	−0.170	−0.354	C
4	82 12 06 06	4.75	−0.234	−0.465	A B C	24	89 11 28 12	6.25	−0.167	−0.464	A C
5	93 11 20 12	5.00	−0.234	−0.541	A B C	25	87 01 11 12	5.75	−0.163	−0.419	B C
6	83 01 21 06	6.25	−0.231	−0.651		26	83 11 24 00	4.75	−0.162	−0.348	A
7	95 02 05 18	6.25	−0.226	−0.557	C	27	84 11 26 12	6.50	−0.161	−0.427	A B
8	93 12 21 18	5.25	−0.205	−0.405	A C	28	86 01 26 00	5.00	−0.160	−0.402	B C
9	91 12 18 18	5.75	−0.203	−0.432	A	29	88 02 03 00	3.75	−0.158	−0.293	A B
10	87 02 25 06	5.00	−0.202	−0.358	A	30	95 10 15 06	3.50	−0.154	−0.298	C
11	84 12 13 18	5.50	−0.201	−0.547	B	31	87 12 30 06	3.75	−0.153	−0.305	B
12	82 01 18 18	3.75	−0.199	−0.358	A B	32	82 04 03 06	5.00	−0.153	−0.378	B C
13	84 02 04 06	5.50	−0.196	−0.401	C	33	90 02 18 12	3.00	−0.153	−0.305	
14	86 01 05 00	5.00	−0.191	−0.379	A C	34	94 11 05 00	3.50	−0.150	−0.314	A C
15	87 04 01 06	4.00	−0.190	−0.338	B C	35	79 11 29 12	5.75	−0.150	−0.402	A
16	91 02 15 18	4.75	−0.188	−0.469	A C	36	94 03 09 00	8.00	−0.149	−0.511	A
17	83 12 21 12	4.25	−0.183	−0.365	B	37	83 01 24 18	5.00	−0.147	−0.311	C
18	90 02 16 06	3.25	−0.178	−0.290		38	82 04 07 00	4.00	−0.146	−0.331	A
19	86 12 08 18	4.50	−0.174	−0.334	B	39	88 04 17 00	3.75	−0.146	−0.344	C
20	84 01 12 06	6.50	−0.172	−0.432	B	40	95 01 15 06	4.50	−0.145	−0.406	

APE collapse defined as APE depletion events with maximum APE fall ($\Delta\mathrm{APE}_{\min}$) $< -0.280 \times 10^6$ J m^{-2} and maximum APE depletion rate ($\mathrm{d}A/\mathrm{d}t_{\min}$) $< -0.145 \times 10^6$ J m^{-2} day^{-1} 1 February 1979–30 November 1995. Listed is time in Greenwich Mean Time (year, month, day, and hour) of $\mathrm{d}A/\mathrm{d}t_{\min}$ ($T=0$), duration of APE collapse (ΔT), maximum APE fall, maximum APE depletion rate, and associated regional synoptic patterns.

[1] Case studies identified in Fig. 3.

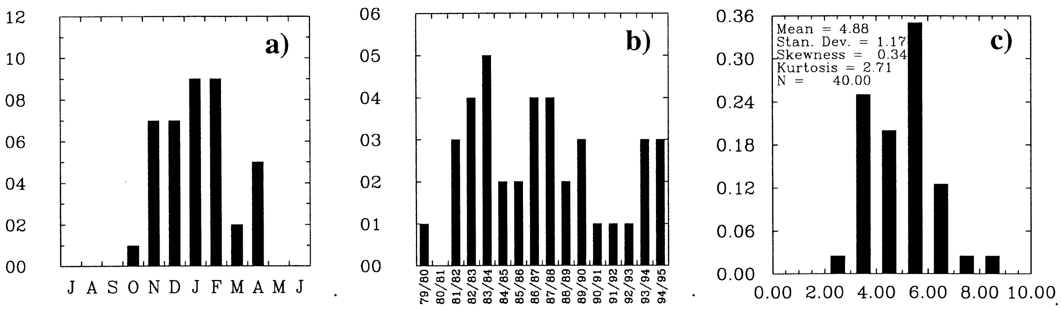

Fig. 4. (a) Monthly climatological frequency and (b) cold-season frequency of Northern Hemisphere APE collapses listed in Table 1.

deviation of the sample. Fig. 5a shows a 0.4×10^6 J m^2 (8%) drop relative to a mean cold-season background level of 5.16×10^6 J m^2. APE depletion occurs over a period of 5 days (Fig. 5b), with half of this fall focussed in the 24 h of maximum APE depletion at $T=0$. The permanent depletion of APE during these 20 days suggests that the synoptic-scale development described in this study is associated with a transition from a high APE to a low APE regime.

4. Regional synoptic structure

4.1. Methodology

Inspection of the 40-case composite (not shown) for 1000–500 and 500–200 hPa thickness and 1000 and 500 hPa heights revealed highly smeared global composites. Manually classifying cases according to observed patterns of regional baroclinic development produced composites more representative of individual cases. Analysis

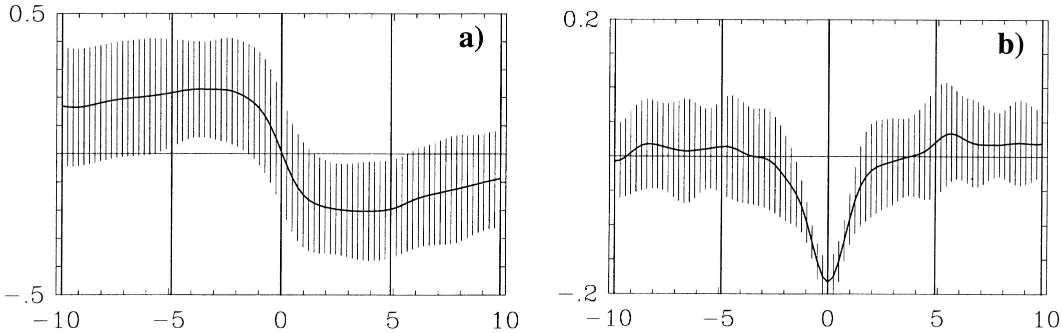

Fig. 5. Composite 20-day time series of (a) APE anomaly and (b) APE generation rate for Northern Hemisphere APE collapses. Centered on time of maximum APE depletion rate dA/dt_{min} ($T = 0$). Anomaly defined as departure from seasonal signal ($T < 180$ days). Error bars denote standard deviation of 40-case sample.

revealed 3 regional patterns of synoptic development dominated by midlatitude thermal surges: Type (A) West Pacific warm surge; Type (B) Bering warm surge; and Type (C) Atlantic Canada warm surge. Specific locations discussed in the text are shown in Fig. 6.

We establish more objective criteria to isolate these synoptic patterns in order to generate reproducible results that are similar to the manual classification. Cases were identified as warm surges if regional zonal gradients of 1000 hPa height (Δz_{1000}) exceeded threshold values at any time between $T = -1$ day and $T = +1$ day, indicating a strong southerly component of the geostrophic wind. Coordinates used to calculate Δz_{1000}, chosen to best duplicate results of the initial manual classification, are shown in Table 2 and plotted in Fig. 6; also shown in Table 2 are threshold values of Δz_{1000}.

Thereshold values are based on a 1979/80–1994/95 cold-season climatology of Δz_{1000}. They are chosen so that the probability of randomly choosing a 2-day period with a Δz_{1000} greater than the regional threshold is 22.5%. A 2-day period allows for case-to-case variability in time lags between maximum APE collapses and the associated synoptic pattern; the 22.5% expectation value (of the 15, 20, 22.5, and 25% values tested on our 40-case data set) yields the most statistically significant samples according to a χ^2 goodness-of-fit test (Freund, 1971):

$$\chi^2 = \frac{(o_1 - e_1)^2}{e_1} + \frac{(o_2 - e_2)^2}{e_2}, \tag{10}$$

where $o_1(o_2)$ and $e_1(e_2)$ represent, respectively, the observed and expected number of cases with Δz_{1000} greater (less) than the thresholds. Table 1 shows the result of this classification scheme, while Table 2 gives the number of observed cases and confidence levels for each type. Statistical and composite time series analysis of each category yielded results similar to Fig. 5, indicating that no category contributed disproportionately to the 40-case composite APE collapse. Note that 16 cases involve at least 2 regional warm surges, suggesting that hemispheric APE collapses are the result of coincident regional events as well as enhanced local physical processes.

Fig. 7 shows that 1000 hPa height gradients provide a good diagnostic proxy for identifying regions of strong geostrophic warm advection associated with thermal surges. Composite anomalies of thermal advection were calculated using the thermal wind relation (equations 4.1.120 and

Table 2. *Threshold criteria for 3 types of regional thermal surges*

Type	Δz_{1000}	Coordinates		N	Conf.
A	> 129 m	40N, 145E	40N, 165E	19	> 1%
B	> 205 m	55N, 170E	55N, 140W	15	> 5%
C	> 156 m	45N, 70W	45N, 50W	20	> 1%

Shows threshold of 1000 hPa height differences (Δz_{1000}), coordinates used to calculate Δz_{1000}, the number of cases in each category, and their statistical significance. A thermal surge is identified for a given APE collapse if Δz_{1000} exceeds thresholds any time between $T = -1$ day and $T = 1$ day.

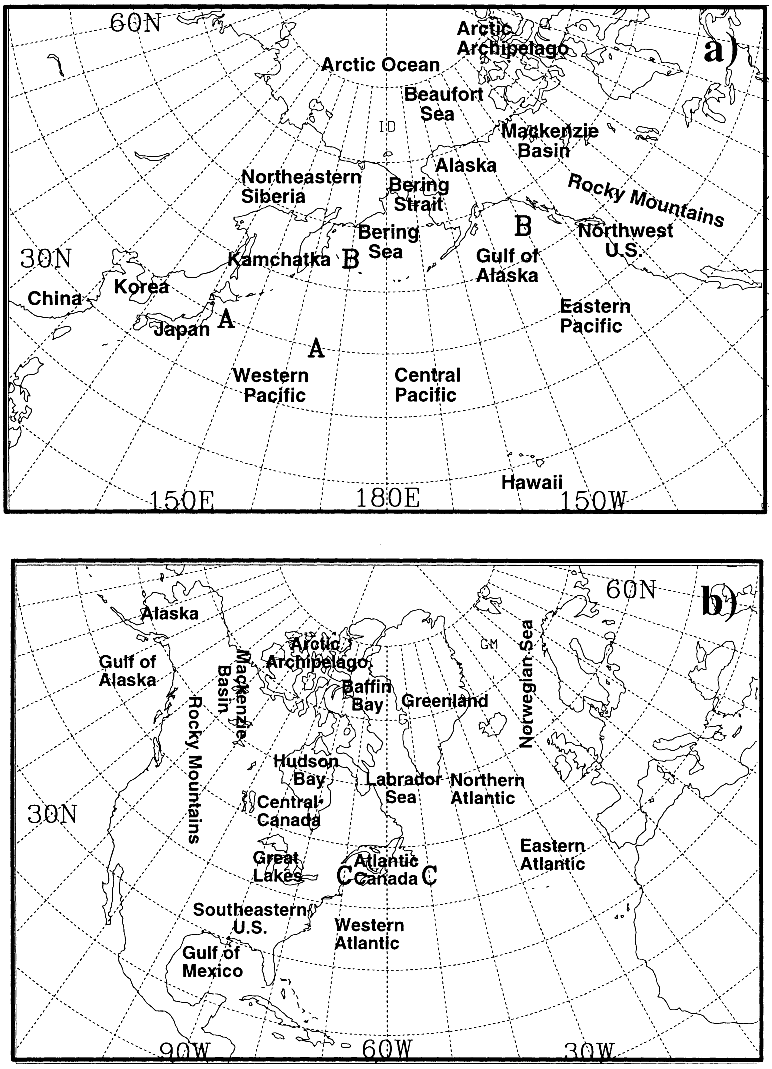

Fig. 6. Locator maps. Letters A, B, and C identify limits of regional warm surges identified in Table 2.

4.1.121, Bluestein, 1992):

$$-v \cdot \nabla T = \frac{f}{R_d} p \left(u_g \frac{\partial v_g}{\partial p} - v_g \frac{\partial u_g}{\partial p} \right), \quad (11)$$

where 850 and 500 hPa heights are used to determine geostrophic wind (u_g, v_g) and shear (du_g/dp, dv_g/dp) at the 675 hPa pseudo-level; geostrophic winds were calculated using a centered-difference formulation:

$$(u_g, v_g) = \frac{g}{f} \left(-\frac{\Delta z_y}{8\Delta y_j}, \frac{\Delta z_x}{8\Delta x_i} \right), \quad (12)$$

where intervals of 8 times the Δx_i and Δy_j grid spacing were chosen to best simulate the scale of the Δz_{1000} thresholds used to identify regional surges. Robust southerly components of geostrophic winds are collocated with the most pronounced deviations from climatological values of 850–500 thermal advection off the coast of Japan (Fig. 7a), near the Bering Sea (Fig. 7b), and over Atlantic Canada (Fig. 7c).

The prominence of synoptic-scale thermal surges is consistent with the strong baroclinic energy conversions during APE collapses predicted by theory. Quasi-geostrophic ascent (descent) in regions of exceptional warm (cold) advection establish both the vertical motions and amplified perturbations necessary for the enhanced thermally direct circulations implicit in the baroclinic conversion term $\omega\alpha$. We analyze results by comparing representative cases identified in Fig. 3 with their respective regional composites.

4.2. *Type A (West Pacific warm surge): representative case and composite (N = 19)*

Fig. 8 shows the representative case of the West Pacific warm surge. A cyclone deepens over Northern Japan, moving northeastward to the southern tip of Kamchatka before stalling. It advects cold air over the Sea of Japan in tandem with an East Asian ridge that decays as it reaches the coast. Over the western Pacific, warm air surges from the subtropical Pacific to the Siberian coast along a channel defined by both the developing cyclone and a ridge over the Pacific. The ridge extends from an anticyclone centered over the Aleutian islands and moves eastward to longitude 180° by $T = +1$ (Fig. 8c). Northerly flow ahead of the ridge taps into a massive cold pool of air over the Bering sea, advecting cold air into the subtropical Pacific. Note that the zonal thermal flow over the western Pacific at $T = -1$ (Fig. 8a) has been strongly deformed by these baroclinic eddies by $T = +1$ (Fig. 8c). In particular, a strong tropospheric thermal ridge forms in the warm flow ahead of the cyclone by $T = 0$ (Fig. 8b). The 2-day thermal tendency (Fig. 9) during this period shows

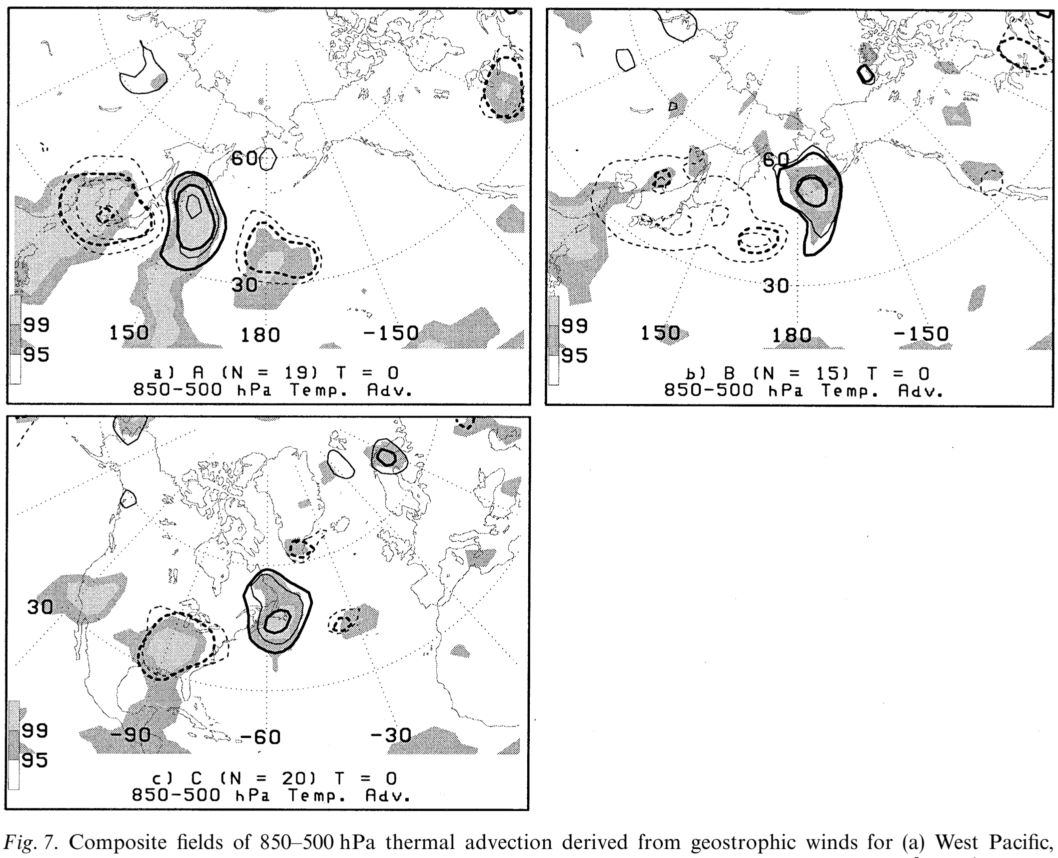

Fig. 7. Composite fields of 850–500 hPa thermal advection derived from geostrophic winds for (a) West Pacific, (b) Bering, and (c) Atlantic Canada warm surges. Contours show composite (thin, interval 3×10^{-5} K s^{-1}, dashed negative), anomaly (bold, interval 3×10^{-5} K s^{-1}, dashed negative), and statistical significance fields as determined by the Student *t*-test (shading, 95% and 99% confidence limits).

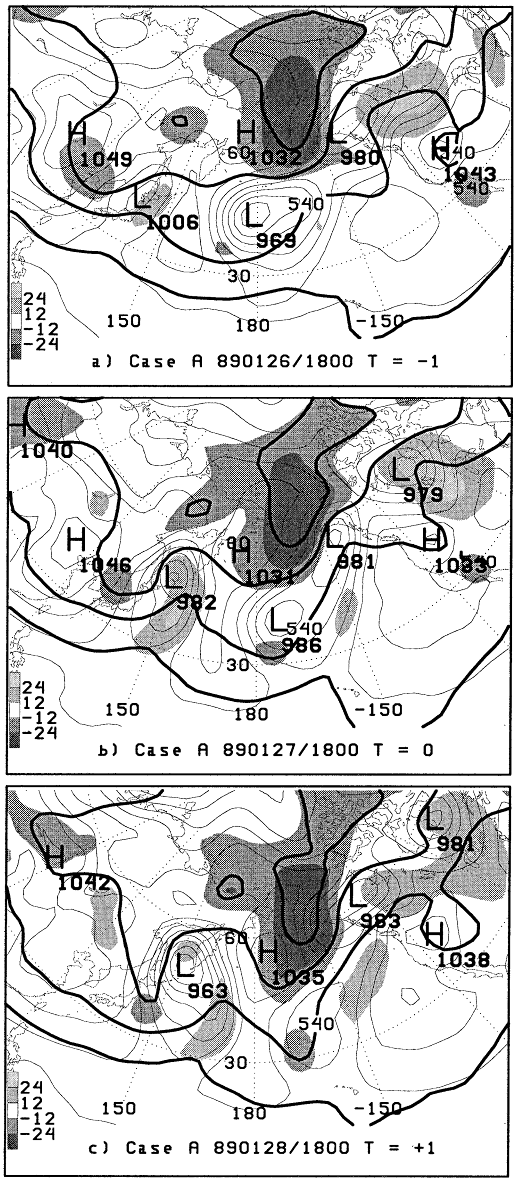

Fig. 8. Representative case of Type A baroclinic development associated with Northern Hemisphere APE collapses $T=-1$ day to $T=+1$ day ($T=0$ defined as in Fig. 5). Sea-level pressure (solid, contour interval 8 hPa), 1000–500 hPa thickness (bold, interval 30 dam) and 1000–500 hPa thickness anomaly (shaded, interval 12 dam).

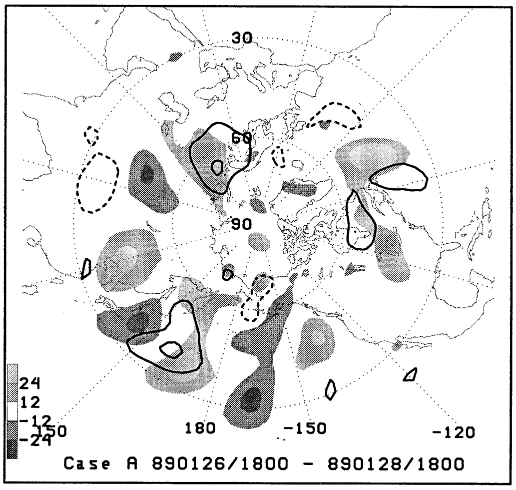

Fig. 9. Thickness tendencies for 2-day periods for Type A case study; 1000–500 hPa (shaded, interval 12 dam) and 500–200 hPa (solid positive, dashed negative, interval 12 dam).

that these features in the western Pacific induce the strongest and most extensive warming and cooling in the hemisphere for this time.

The growth of such a large thermal wave suggests that baroclinic energy conversions in this region play a major rôle in the APE collapse. Fig. 10 shows the 500 hPa baroclinic conversion ($\omega\alpha$) from (2) at $T=0$. The largest negative contri-

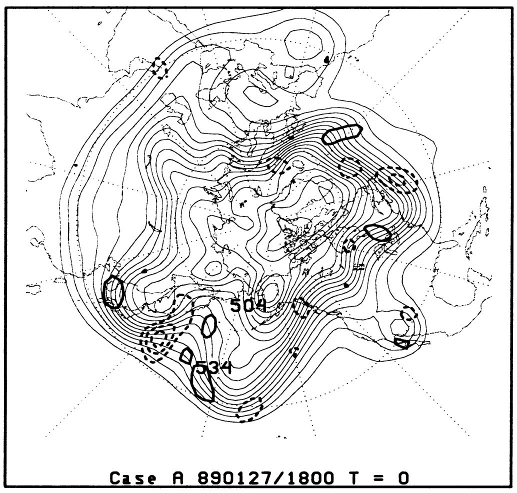

Fig. 10. Geopotential height (light, interval 6 dam) and baroclinic energy conversion $\omega\alpha$ (bold, dashed negative, interval 0.6 W kg^{-1}) at 500 mb.

bution in the hemisphere occurs off the coast of Japan ahead of a 500 hPa trough and above the defining warm surge pictured in Fig. 8b.

Features also appearing in the Type A composite in Fig. 11 include cyclogenesis over Japan (Figs. 11a–c) and a strong warm surge over the western Pacific (Figs. 11d–f). Warming during this period extends well into northeastern Siberia in the upper troposphere (Figs. 11g–i): the warm surge is by far the most prominent feature. To the west, a decaying anticyclone slowly encroaches upon eastern Asia in association with a shallow Asian cold surge, and an anomalous ridge upstream of the cyclone advects cold air from the Bering Sea into the central Pacific.

Baroclinic activity over the west central Pacific appears more prominent in the composites. Fig. 11b shows a closed anticyclone forming in the subtropics over the central Pacific at $T=0$. A deep tropospheric cold anomaly begins to surge southward. Comparison to composite fields of 1000–500 hPa thickness fields (Fig. 11e) shows strong cold advection in the region to the northeast of the anticyclone. Cold advection also takes place in the 500–200 hPa layer as the mean flow aloft (not shown) advects an upper tropospheric cold wave across the Western Pacific (Figs. 11g–i). By $T=+1$, a deep tropospheric cold anomaly dominates the thermal anomaly field in both the upper and lower troposphere (Figs. 11f, i); its intensification induces a thermal wave in both the composite 500–200 and 1000–500 thickness fields.

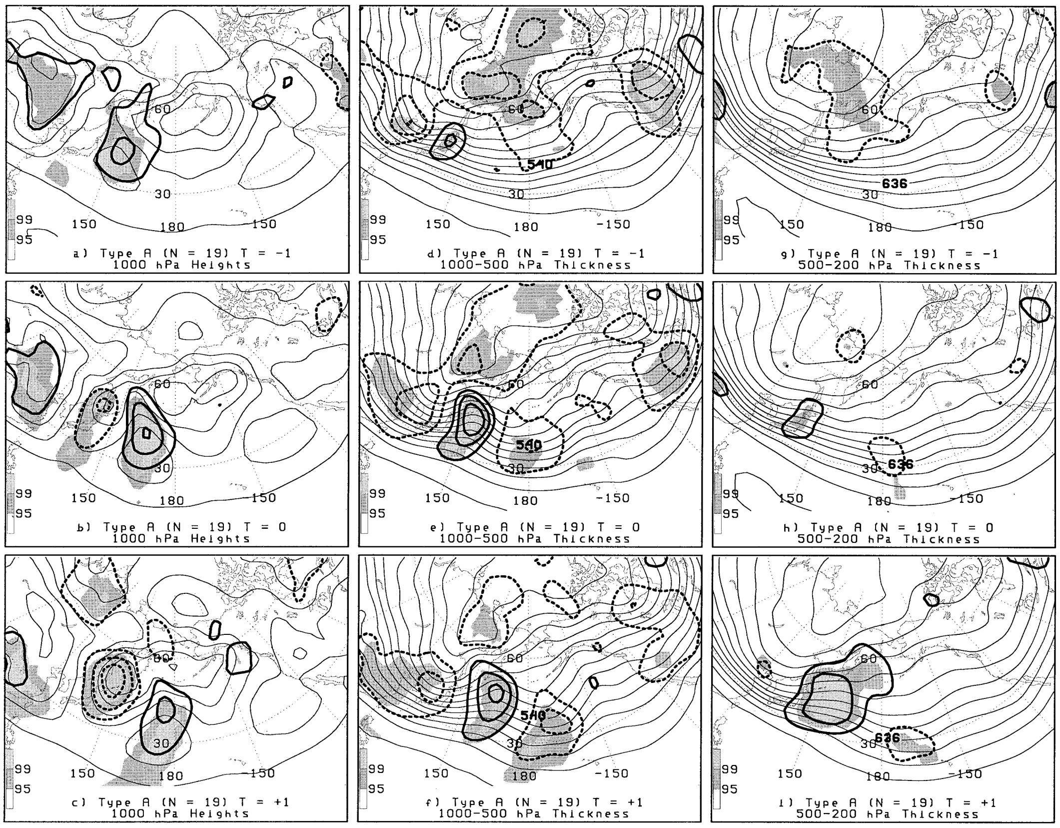

Fig. 11. Composite synoptic structure of APE collapse. Type A: West Pacific warm surge. Fields of 1000 hPa height, 1000–500 hPa thickness, and 500–200 hPa thickness at $T=-1$, $T=0$, and $T=+1$ day. Contours show composite (thin, interval 6 dam, interval 4 dam for 1000 hPa), anomaly (bold, interval 3 dam, dashed negative), and statistical significance fields as determined by the Student t-test (shading, 95% and 99% confidence limits).

4.3. *Type B (Bering warm surge): representative case and composite ($N = 15$)*

The Bering warm surge in Case B (Fig. 12) shows warm flow across the Bering sea already well established at the onset of the 2 days of strongest APE collapse. At $T = -1$, Fig. 12a shows a 1068 hPa anticyclone over Alaska and a 986 cyclone over Kamchatka combining to produce a southeasterly geostrophic flow across the Bering Sea. Southerly geostrophic flow into the Bering Sea intensifies over the next 2 days.

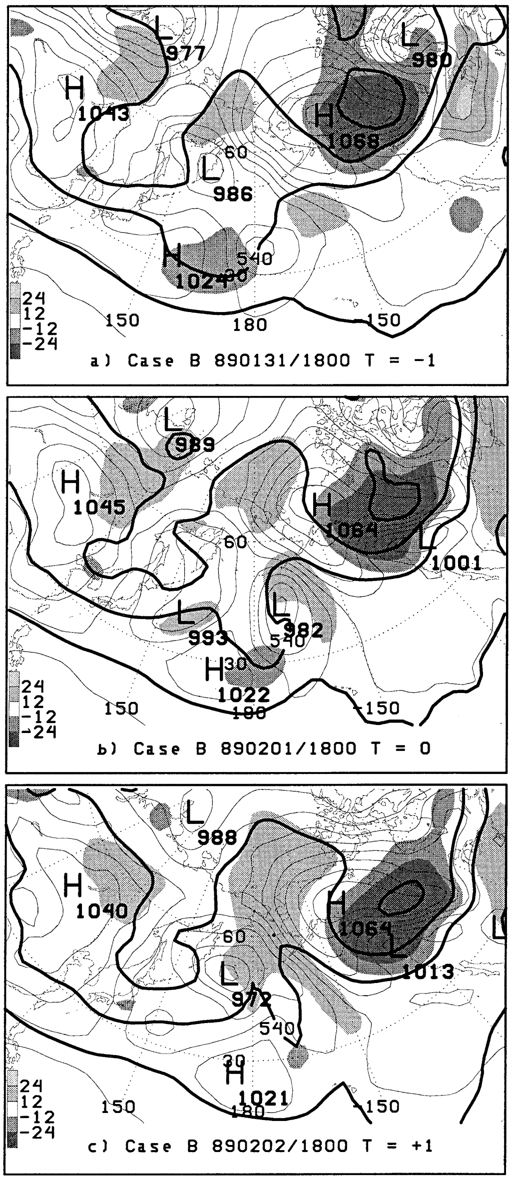

Fig. 12. Case B: as in Fig. 8, but for Type B (Bering warm surge).

Fig. 12b shows warm air wrapping around the surface ridge into the northern Mackenzie Basin at $T = 0$; the 510 dam thickness contour lies along the western coast of the Arctic Archipelago by $T = +1$ (Fig. 12c). A large thermal wave (5000 km wavelength) defined by the arctic warm surge and adjacent cold pools amplifies along this contour. Cyclogenesis in the central Pacific supplies an extra surge of subtropical air into the Bering Sea, with a 982 hPa cyclone amplifying the midlatitude thermal wave in the 540 dam contour at $T = 0$ (Fig. 12b). This system merges with an incipient cyclone over the western Pacific and a stationary system over Kamchatka to produce an elongated trough that extends all the way to Hawaii (Fig. 12c).

Farther east at $T = -1$, ridges in the sea-level pressure field extend from an anticyclone center over eastern Alaska into the Mackenzie Basin and the Gulf of Alaska (Fig. 12a). This anticyclone set the North American record for reduced sea-level pressure, with Northway Alaska reporting 1076 hPa at 0000 UTC 1 February (Tyle, 1995). It evolved from the Aleutian ridge of Case A (Fig. 8), undergoing rapid intensification as it moved across the Bering Sea and into Alaska (Tan and Curry, 1993). The intense arctic cold pool has also moved eastward, now residing over the Mackenzie Basin (Fig. 12a). In conjunction with a stationary sea-level depression near Kamchatka, it sustains the massive flow of warm air into the Arctic via the Bering Strait and Alaska (Tanaka and Milkovich, 1990).

Fig. 13 shows thermal surges associated with these systems dominating the hemisphere during this period. The Alaska anticyclone is associated with intense warming (cooling) to the west (east) of the circulation center. Over the western and central Pacific, the dual cyclogenesis coincides with a tripole pattern involving a warm surge flanked by 2 cold surges.

The composite case of 16 Bering warm surges shows similar deep tropospheric warming over the Bering Sea, with the upper-level warming (Fig. 14g–i) occurring slightly to the west of the lower tropospheric warm surge (Fig. 14d–f). The

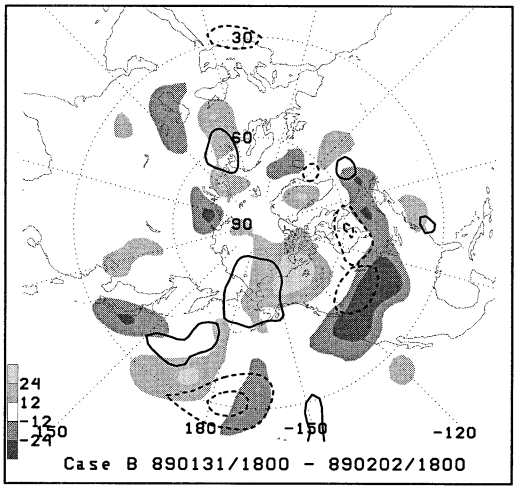

Fig. 13. As in Fig. 9, but for Type B.

warming is unambiguously associated with the warm flow between the intense Kamchatka cyclone and the ridge extending into the Gulf of Alaska; by $T = +1$ day, a prominent thermal wave appears in the region of the Bering Sea in the lower and upper troposphere (Figs. 14f, i).

The sea-level pressure field of the case study (Fig. 12) shows the eastern arm of the Alaska anticyclone extending progressively southward in the lee of the Rockies. A 1001 hPa low develops a closed circulation over the northwestern US by $T = 0$, enhancing the north–south pressure gradient over much of western Canada (Fig. 12b). Fig. 13 shows that the cold air surges southward along this gradient into the western half of the US and adjacent Pacific, suggesting that cross-isobaric circulations play a large rôle in the baroclinic development of this pattern. In the composite field, the eastern arm of the Alaska anticyclone extends into the lee of the Rockies (Figs. 14a–c),

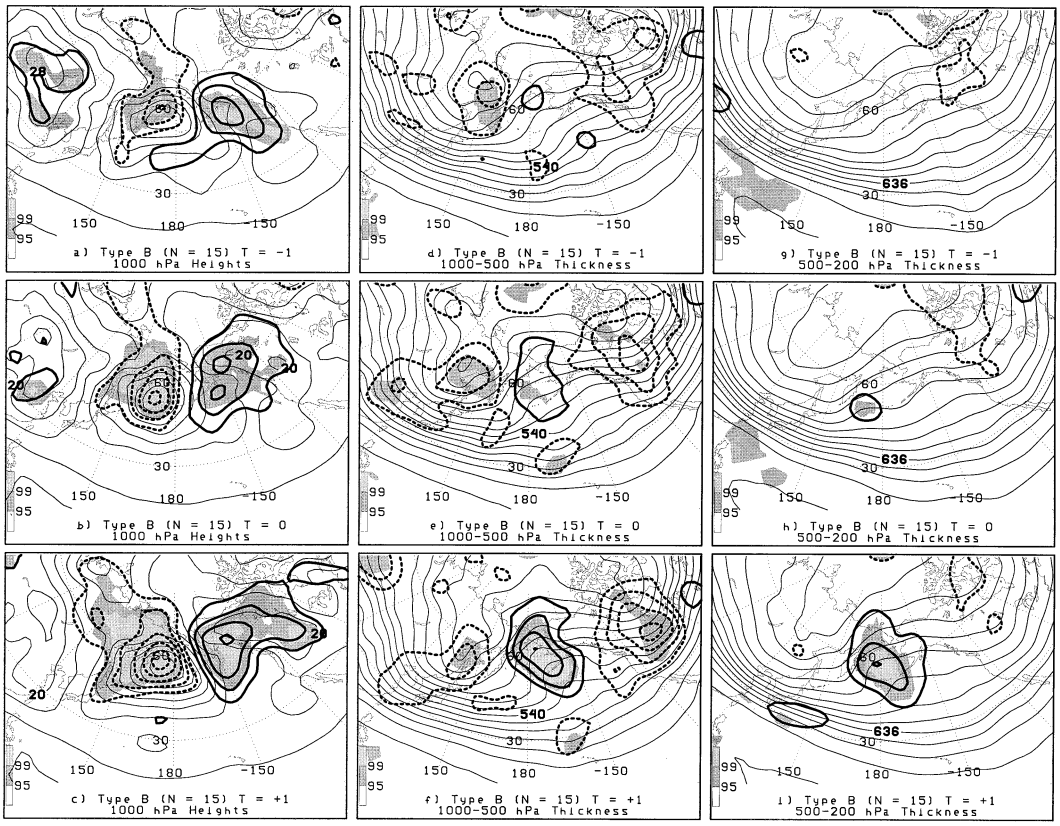

Fig. 14. As in Fig. 11, but for Type B.

but without a significant cold surge (Figs. 14d–f): cases associated exclusively with Kamchatka cyclones smear this feature considerably.

The signal in the early stages of the APE collapse is not as clear as with the other composites. Inspection of individual cases shows that the dynamical structures transporting warm air into the Bering Sea vary from case to case, smearing the composites. For example, the 1000 hPa composites show a southwesterly geostrophic flow into the Bering Sea at $T = -1$ and $T = 0$ (Figs. 14a, b) associated with an incipient Kamchatka cyclone and elevated height anomalies just south of the Bering Sea. Although cyclogenesis in the western Pacific induces a similar feature in the case study (Fig. 12c), the warm southeasterly flow into the Bering Sea is more prominent throughout the 2-day period.

4.4. *Type C (Atlantic Canada warm surge): representative case and composite ($N = 20$)*

The March 1993 Superstorm (SS93) that originally motivated this investigation is a classic example of the Type C pattern of development. At $T = -1$, Fig. 15a shows a large cold anomaly associated with cold advection over much of North America. Northerly flow west of a family of North Atlantic cyclones advects some of this air over Atlantic Canada between $T = -1$ and $T = 0$, so that a broad baroclinic zone extends from western North America to the central Atlantic Ocean (Fig. 15b). By $T = +1$, the rapidly intensifying storm deforms this zonal pattern, with a warm surge carving out a strong thermal ridge over Atlantic Canada (Fig. 15c). An anticyclone moves southward from the western US to the Gulf of Mexico, contributing to an intense cold surge that extends into Central America (Schultz et al., 1997). A 1000 hPa ridge also amplifies ahead of the storm. It combines with the upstream cyclone to intensify the warm onshore flow and with a downstream system to advect cold air across the Labrador Sea into the Atlantic.

It is the warm surge that has the most dramatic impact upon the thermal field. Fig. 16 shows the intense warming over Atlantic Canada in both the upper and lower troposphere; the cold surges, while impressive, are less prominent in the upper troposphere. Significant deep tropospheric warming over Scandinavia and in the Arctic north of

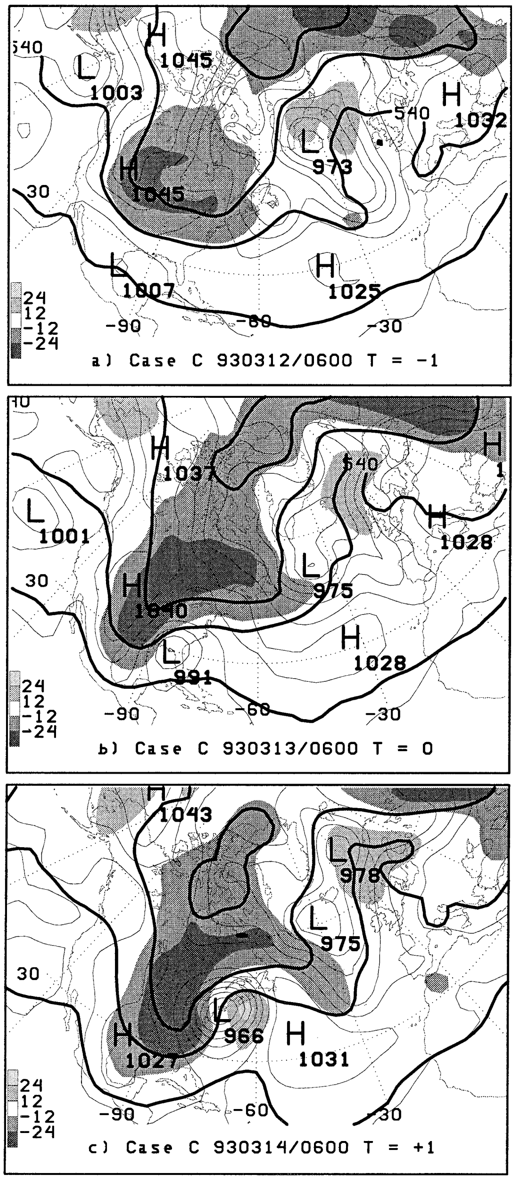

Fig. 15. Case C: as in Fig. 8, but for Type C (Atlantic Canada warm surge).

Siberia probably acts simultaneously to reduce the global APE.

Warming in the upper troposphere is of particular interest. In the case of SS93, Huo et al. (1995) suggest that upper-tropospheric latent-heat release in the warm sector contributes to cyclone

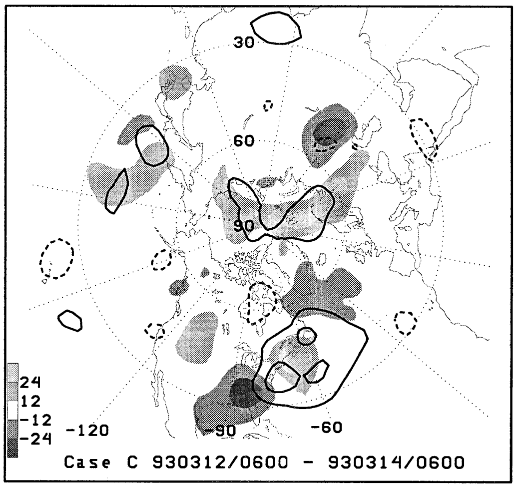

Fig. 16. As in Fig. 9, but for Type C.

deepening more efficiently than at lower levels. This is consistent with climatological studies by Siegmund (1994), who shows that the planetary APE is especially sensitive to upper troposphere diabatic heating in the high and middle latitudes via the efficiency factor in (3). Siegmund (1995) suggests that high generation rates of transient APE in GCMs are linked to the misplacement of latent heating within transient warm anomalies when the models do not resolve the mesoscale features associated with storm development.

Fig. 17 shows that Atlantic Canada warm surge development is generalized over 18 cases of Type C APE collapse. At $T=-1$, significant cold anomalies reside south of Newfoundland in both the 1000–500 and 500–200 hPa layers (Figs. 17d, g). These define an anomalously zonal flow over much of the eastern Atlantic. By $T=-1$, these anomalies have translated eastward, replaced by large warm anomalies (Figs. 17f, i). The composite fields at this time show the development of a distinct baroclinic wave, with a trough axis extending from Hudson Bay to the Gulf of Mexico, and a ridge axis spanning the northern tip of Labrador, Newfoundland and the western Atlantic.

The features of the 1000 hPa height composites (Figs. 17a–c) are consistent with the observed development of SS93, leading the overall pattern by about $\frac{1}{2}$ day. The intensification over eastern North America of an elongated trough reflects the various storm tracks represented here. Whereas the closed circulation associated with the composite moves from the Great Lakes to Atlantic Canada, many of these cyclones in fact follow a more southerly or northerly track. As with SS93, an anticyclone weakens as it tracks from the western US to the Gulf of Mexico in the wake of a cold surge, while a ridge extends from the central Atlantic to the tip of Greenland. Each of these eddies contributes to the evolution of the thermal field as in the case study.

5. Conclusions

A 1979–95 time series of intraseasonal Northern Hemisphere available potential energy (APE) is used to objectively define a data set of exceptional synoptic-scale APE collapses. Data are derived from the National Centers for Environmental Prediction (NCEP) reanalysis. Transient synoptic structures associated with APE collapses are identified. We propose that such events have a disproportionate effect on the hemispheric circulation, and that their associated regional synoptic structure should therefore be of practical and theoretical interest in studies of climate, the general circulation, and numerical weather prediction.

The time series is analyzed and filtered using Fourier decomposition. The intraseasonal signal (of 1.6–180 days) accounted for about 3% of the total variance, peaking in the low-frequency range near 30 days. The cold season (15 October–15 April) rms variance (0.20×10^6 J m^{-2}) is more than double that of the warm season (15 April–15 October) value (0.11×10^6 J m^{-2}), and exhibits considerable interannual variability.

We identify an average cycle of approximately 3 days in the APE generation rate dA/dt (referred to as APE depletion rate if negative) using the intraseasonal time series. APE depletion events are defined as individual falls and rises in dA/dt, their onset and termination defined by adjacent peaks in dA/dt. Their time scale is consistent with that of baroclinic instability and observations of developing synoptic eddies. Synoptic-scale APE collapses are defined as events with APE depletion rates (dA/dt_{min}) and maximum APE falls ΔA_{min} less than -0.145×10^6 J m^{-2} day^{-1} and -0.280×10^6 J m^{-2}, respectively. They are randomly distributed among the different cold seasons

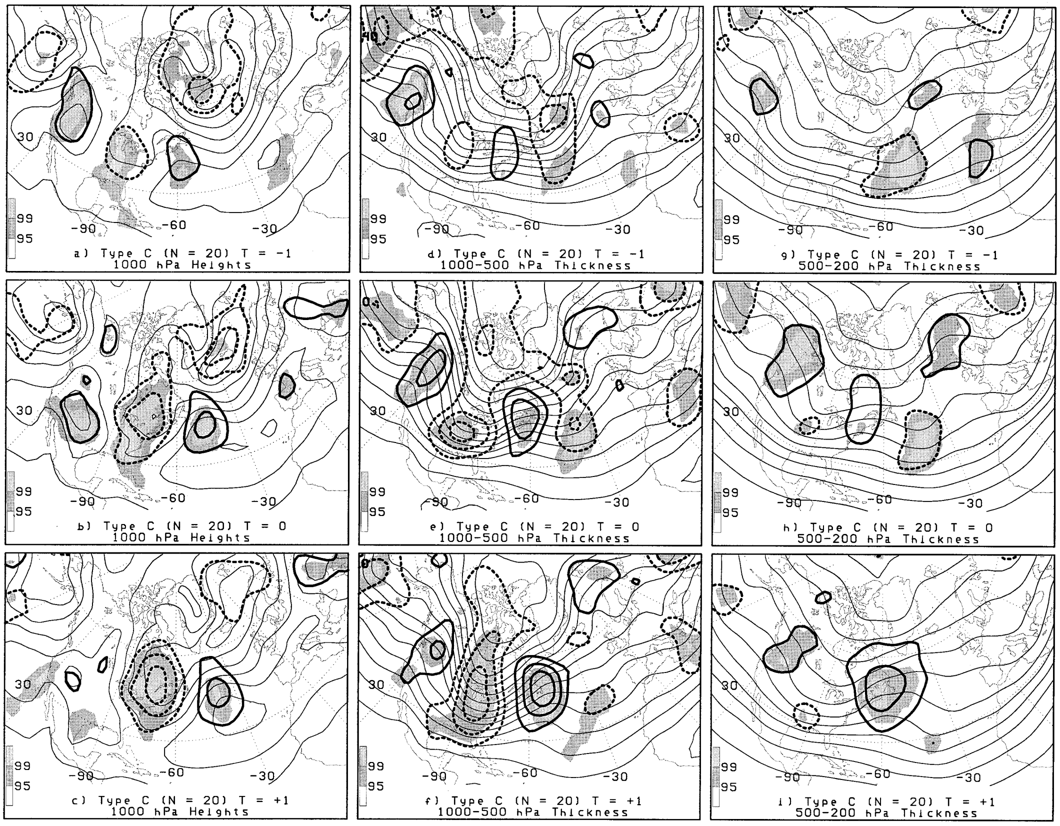

Fig. 17. As in Fig. 11, but for Type C.

with a preference for colder months, persisting 2 days longer than the typical APE depletion event.

APE collapses are classified into 3 types based on the evolution of regional synoptic patterns during the 2 days centered on $T = 0$ (the time of dA/dt_{min}). About half of these cases involve the simultaneous appearance of more than one of the identified regional structures. All regional signatures are defined by a deep tropospheric surge of warm marine air associated with intensifying synoptic-scale eddies. The warm surges represent the major factor in the deformation of a zonal flow into a baroclinic wave. The west Pacific warm surge (Type A) pattern is accompanied by cyclogenesis over Japan and the formation of a strong ridge over the west-central North Pacific. Also present is a shallow lower-tropospheric cold surge into East Asia, and a deep tropospheric cold surge downstream of the North Pacific anticyclone. The Bering warm surge (Type B) is associated with an intense southerly flow across the Bering Strait. This is accompanied by cyclogenesis near the Kamchatka Peninsula and/or intense anticyclogenesis over Alaska. Both structures play a rôle in the Alaska warm surge of 1989 (Tanaka and Milkovich, 1990), the strongest APE collapse of the study period. The Atlantic Canada warm surge (Type C) is characterized by an onshore flow of warm air and a continental storm track over eastern North America. The strong thermal ridge and a continental cold surge define an amplifying baroclinic wave. The March 1993 Superstorm (Bosart et al., 1996) that motivated this study is representative of Type C patterns.

The prominence of upper tropospheric warming in regions of strong lower-tropospheric warm advection suggests that latent heating plays a key rôle in generating local APE and enhancing the thermally direct circulations that accompany developing baroclinic systems (Huo et al., 1995, Siegmund, 1995). Future work will focus on thermodynamic and energy budgets of representative cases, with particular emphasis on quantifying the rôle of diabatic and baroclinic processes associated with thermal surges.

6. Acknowledgements

This research has been sponsored by the Natural Sciences and Engineering Research Council (NSERC), the Atmospheric Environment Service of Canada and the NSERC research partnership support of the Mackenzie GEWEX study. We wish to thank the Climate Diagnostics Center for providing the NCEP reanalysis data, and Rick Danielson and Marco Carrera for revising drafts of the manuscript.

REFERENCES

Bluestein, H. B. 1992. *Synoptic-dynamic meteorology in midlatitudes.* Volume I: *Principles of kinematics and dynamics.* Oxford University Press, 421 pp.

Bosart, L. F., Hakim, G. J., Tyle, K. R., Bedrick, M. A., Bracken, W. E., Dickinson, M. J. and Schultz, D. M. 1996. Large-scale antecedent conditions associated with the 12–14 March 1993 Cyclone ("Superstorm '93") over Eastern North America. *Mon. Wea. Rev.* **124**, 1865–1891.

Dutton, J. A. and Johnson, D. R. 1967. The theory of available potential energy and a variariational approach to atmospheric energetics. *Adv. in Geophys.* **12** (Academic Press), pp. 333–436.

Freund, J. E. 1971. *Mathematical statistics.* Prentice-Hall, 463 pp.

Huo, Z.-H., Zhang, D. H., Gyakum, J. R. and Staniforth, A. 1995. A diagnostic study analysis of the Superstorm of March 1993. *Mon. Wea. Rev.* **123**, 1740–1761.

Kalnay, E., Kanamitsu, M., Kistler, R, Collins, W., Deaven, D., Gandin, L., Iredell, M., Saha, S., White, G., Woollen, J., Zhu, Y., Cheliah, M., Ebisuzaki, W., Higgins, W., Janowiak, J., Mo, K. C., Ropelewski, C., Wang, J., Leetma, A., Reynolds, R., Jenne, R. and Joseph, D. 1996. The NCEP/NCAR 40-year reanalysis project. *Bull. Amer. Meteor. Soc.* **77**, 437–471.

Lin, S. C. and Smith, P. J. 1982. The available potential energy budget of a severe storm-producing extratropical cyclone. *Mon. Wea. Rev.* **110**, 521–533.

Lorenz, E. N. 1955. Available potential energy and the maintenance of the general circulation. *Tellus* **7**, 157–167.

Margules, M. 1903. Über die energie der sturme. *Jahrb. Zentralanst. Meteor.*, 1–26 (Translation by C. Abbe (1910) in *Smithsonian Institute Miscellaneous Collection* **51**, 553–595).

Orlanski, I. and Sheldon, J. P. 1995. Stages in the energetics of baroclinic systems. *Tellus* **47A**, 605–628.

Peixoto, J. P. and Oort, A. H. 1992. *Physics of climate.* American Institute of Physics, 520 pp.

Schultz, D. M., Bracken, W. E., Bosart, L. F., Hakim, G. J., Bedrick, M. A., Dickinson, M. J. and Tyle, K. R. 1997. The 1993 Superstorm cold surge: frontal structure, gap flow, and tropical impact. *Mon. Wea. Rev.* **125**, 5–39; Corrigendum **125**, 662.

Sheng, J. and Derome J. 1991. An observational study of the energy transfer between the seasonal mean flow and transient eddies. *Tellus* **43A**, 128–144.

Siegmund, P. 1994. The generation of available potential energy, according to Lorenz's exact and approximate equations. *Tellus* **46A**, 566–582.

Siegmund, P. 1995. The generation of available potential energy: a comparison of results from a general circulation model. *Climate Dynamics* **11**, 129–140.

Smith, P. J. 1969. On the contribution of a limited region to the global energy budget. *Tellus* **21**, 202–207.

Tan, Y.-C. and Curry, J. A. 1993. A diagnostic study of the evolution of an intense North American anticyclone during winter 1989. *Mon. Wea. Rev.* **121**, 961–975.

Tanaka, H. L. and Milkovich, M. F. 1990. A heat budget analysis of the polar troposphere in and around Alaska during the abnormal winter of 1988/89. *Mon. Wea. Rev.* **118**, 1628–1639.

Trenberth, K. E. and Olson, J. G. 1988. An evaluation of global analyses from the National Meteorological Center and European Center for Medium Range Weather Forecasts. *Bull. Amer. Meteor. Soc.* **69**, 1047–1057.

Tolstov, G. P. 1962. Fourier series. Dover Publications, 336 pp.

Tyle, K. R. 1995. Intense surface anticyclogenesis: climatology and composite/individual case studies. M.Sc. Thesis, State University of New York, Albany.